Study on Oil-Water Two-phase Flow in the Invisible Measuring Pipeline of the Horizontal Tri-electrode Capacitive Sensor

Lei Li, Ming Wang*, Dahai Wang, Xuewei Gao, Qianhui Zhu

School of Information and Electronic Engineering, Shandong Technology and Business University, *Binhai Zhong Road*, No. 264000, Yantai, China, *1099162031@qq.com*

Abstract: Based on the well logging requirements of horizontal stripper wells, the flow characteristics of the oil-water two-phase flow in the invisible horizontal tri-electrode capacitive sensor (HTCS) measurement pipeline are studied. First, an experimental device and a numerical validation model of a horizontal 20 mm glass pipeline are established to study the flow characteristics of the oil-water two-phase flow. Then, the flow characteristics of the horizontal oil-water two-phase flow in the measurement pipeline under different horizontal inclination angles are studied and the flow patterns and inclination angles suitable for the new tri-electrode capacitive sensor are discussed. Finally, using the horizontal oil-water two-phase flow loop platform of the largest oil and gas testing center in China, the dynamic response of the new capacitive sensor is studied under different inclination angles, flow rates, and water-cut conditions, and the dynamic response law is analyzed based on the simulation results.

Keywords: Horizontal oil-water two-phase flow, invisible, flow characteristics, capacitive sensor, water content.

1. INTRODUCTION

Horizontal well-mining technology is known as the second revolution in the oil industry. The increasing maturity of horizontal well completion has become the key technology to increase the low permeability, thin oil layer production, difficult-to-exploit remaining oil fields, and unconventional oil fields.

However, water immersion will greatly affect the development of horizontal wells after continuous exploitation. Thus, the key to reasonable formulation of water plugging and fracturing plans is to obtain logging information on the horizontal well production profiles [1].

In horizontal and near-horizontal oil wells, the flow state, flow velocity, and the concentration profile distribution are extremely complex. Flow patterns include laminar flow with separate heavy and light phases, undulating flow, upper and lower laminar dispersion flow, and full spatial dispersion flow patterns, and even the flow patterns are strongly influenced by well slope. The complex changes in the flow patterns have a great impact on the response characteristics of downhole water content measurement sensors [2], [3]. It is therefore very important to study the flow characteristics of the oil-water two-phase flow in horizontal measurement pipelines.

In the 1980s, researchers began to carry out studies on oil-water two-phase flow in near-horizontal tubes, focusing on oil-water two-phase flow and gas-liquid two-phase flow [4], [5]. For horizontal oil-water two-phase flow, early researchers mainly carried out experimental studies on the flow characteristics of the horizontal oil-water two-phase flow in small glass or Plexiglas tubes [6], [7]. Tan et al. carried out oil-water two-phase flow experiments in a horizontal tube with a diameter of 14.6 mm using a high-speed camera method to investigate the effects of oil-phase viscosity, tube diameter, and material of pipeline on the fluid flow patterns [8]. Jin et al. conducted an experimental study on the flow characteristics of the horizontal oil-water two-phase flow in a horizontal pipe with an inner diameter of 20 mm, using an 8-channel radial microconidia-activity probe, a fast-closing valve method, and a capacitance probe [9]. Zhai et al. proposed a conductivity parallel line array probe for measuring oil-water interface properties in horizontal oil-water two-phase separation flow regimes, and the sensor was able to detect the interface height at different locations in the tube cross-section and reconstruct a three-dimensional image [10]. Luo et al. carried out an experimental study of extra thick oil-water two-phase flow in a horizontal tube, and the experiment used microscopic camera technology to obtain six flow patterns and summarized the two-phase flow pattern of extra thick oil-water at 80°C [11]. He et al. acquired multi-channel signals from a rotating electric field conductivity sensor with eight electrodes in a pipe with an inner diameter of 20 mm and recorded typical low-mode images with a high-speed camera [12]. Qing et al. used impedance spectroscopy to detect oil-

Corresponding author: 1099162031@qq.com (Ming Wang)

water emulsions with different water content. The diffusion frequency extracted from impedance spectroscopy was linearly related to the water content of the emulsion [13]. Yang et al. established a new oil-water two-phase flow shearwater prediction model using the microwave resonant cavity method and the analytical field solution method [14]. Liu et al. proposed a dual-mode sensor combining a CWUD sensor and a conductivity sensor for identifying flow patterns in horizontal oil-water two-phase flows. The overall identification accuracy of the horizontal oil-water two-phase flow was 94.74% by Doppler spectral analysis and feature extraction from conductivity parameters [15]. Su et al. studied the flow interaction and proposed a model for phase fraction measurement based on ultrasonic transmission. The results show accurate detection of the gas-liquid interface and the phase fractions of oil, gas, and water [16]. Bai et al. proposed a nonlinear analysis method based on the fractional entropy algorithm to characterize and differentiate the patterns of low-speed and high-water-cut oil-water two-phase flow [17].

In addition to the experimental studies on horizontal oil-water two-phase flow, studies on the computational fluid dynamics simulation of oil-water two-phase flow have also made great progress with the development of computer technology [18], [19]. Shi et al. used FLUENT to numerically simulate various flow patterns of horizontal oil-water two-phase flow and studied the effects of turbulence scheme and wall contact angle on the simulation results in the case of annular flow [20]. Gu et al. studied the flow patterns and local phase volume fraction in a horizontal pipe with an inner diameter of 20 mm, used simulation software to calculate the local oil cut, and finally verified the reliability of numerical simulation to extract the local oil-cut in a horizontal oil-water two-phase flow pipeline through experiments [21]. Gao simulated the stratified turbulent oil-water two-phase flow in a horizontal pipe by numerical simulation and concluded that the pressure loss at different flow rates, viscosities, and densities mainly depends on the flow ratio and the physical properties of the fluid [22]. Desamala et al. used the CFD simulation software to analyze the flow pattern diagram, volume fraction, radial pressure distribution, and velocity of oil and water phases in a horizontal pipeline, and successfully predicted almost all flow patterns except oil dispersion in water and water dispersion in oil by simulation, and the simulation results agreed with the experimental results [23], [24]. Li et al. investigated the flow pattern of oleic acid-water microfluidics in a pipeline with a width of 240 microns and a depth of 8 microns. The study focused on the transition between parallel flow and other flow patterns, suggesting that liquid-solid interaction regulates the flow pattern under small Reynolds number conditions [25]. Daneshvar Garmroodi et al. investigated the flow of a waxy crude oil-water layer in a horizontal pipeline using a three-dimensional numerical approach, including the effects of the contraction-expansion device and the pipeline wall heat flux on the pressure drop and two-phase flow [26]. Mazza et al. conducted experiments in a 26 mm diameter pipe using a local impedance probe and a high-speed film to determine the flow patterns. Six different flow patterns were identified: dispersed bubbles, core annulus, bubbles, churning turbulence, and elongated water

droplets [27]. Gao et al. developed a unified model for oil-water two-phase flow in complex pipelines based on the theory of pipeline series-parallel connection, the flow pattern conversion criterion, the two-fluid model and the homogeneous model. The highest absolute percentage error of the proposed model is 14.4% and the average error is 9.8% compared to the CFD results for water volume fractions from 0% to 100% [28]. Bochio et al. collected experimental data on pressure drop, volume fraction, and flow patterns for liquid-liquid flow in a high-viscosity score layer. These data were compared with a computational fluid dynamics model using OpenFOAM and a one-dimensional model. The results show good overall results for CFD and experiments in terms of pressure drop, volume fraction and phase distribution [29]. Liu et al. combined an electromagnetic flowmeter with a differential pressure sensor to measure the inclined oil-water flow in a 20 mm pipe. The desired water retention was measured by correlating the two-phase friction factor with the Reynolds number of the mixed fluid [30].

Two-phase flow is affected by complex factors such as fluid turbulence, inter-phase interface interaction, and relative motions between phases, and its flow behavior is highly irregular, random, and structurally unstable. In this paper, we propose to carry out an experimental study on the flow characteristics of the horizontal oil-water two-phase flow in the non-visible NTCS measurement pipeline using the Daqing oilfield horizontal oil-water two-phase flow device and the fluid simulation FLUENT, which can provide a more comprehensive understanding of the flow pattern changes of the oil-water two-phase flow in the non-visible horizontal manifold under different working conditions.

2. NUMERICAL MODEL

The cylindrical capacitance sensor is mainly studied for oil-water stratified fluids, and it is difficult to measure non-stratified fluids. For this situation, a new combined capacitive sensor model has been designed, and its cross-sectional diagram is shown in Fig. 1.
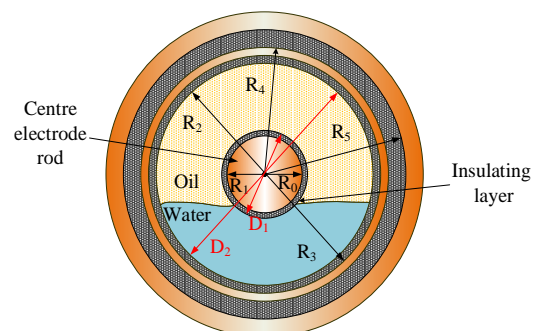

Fig. 1. Cross-section of the new combined capacitive sensor model.

The cylindrical and the coaxial capacitive sensor work together for compensation, extending the response range in stratified flow and increasing the resolution in non-stratified flow by increasing the effective contact area and the adhesion rate of the oil bubble. Fig. 2 shows the equivalent circuit of the combined capacitive sensor in a stratified state.
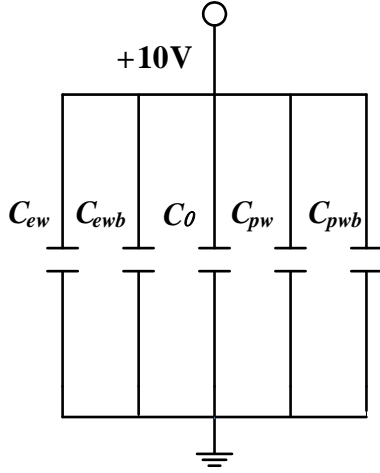
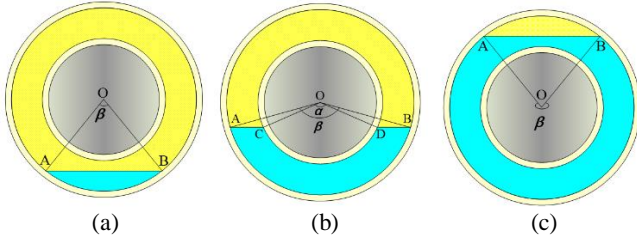Fig. 2. Equivalent circuit of a combined capacitive sensor.

Fig. 3. Internal geometry of a combined capacitance sensor at different oil-water interface heights: (a) Interface lower than electrode rod, (b) Interface contact electrode rod, (c) Interface higher than electrode rod.

The capacitance is composed of five parallel capacitors: the first capacitor is generated by the metal layer electrode, the metal shell and the external insulation layer is referred to as C_0; the second capacitor is generated by the metal layer electrodes, the inner insulation layer and the water in contact with the inner insulation layer and is referred to as C_{ew}; the third capacitor is generated by edge effects near the interface and is denoted as C_{ewb}; the fourth capacitor is generated by the center electrode, the outer insulation layer of the center electrode and the water in contact with them is referred to as C_{pw}; the fifth capacitor is generated by the edge effect near the oil-water interface and is denoted as C_{pwb}. ε is the dielectric constant in the vacuum state, ε_0 is the dielectric constant of the insulation layers and the oil, L is the length of the electrode, α and β are the center angles, which are formed by circles with radii R_1 and R_2 and oil-water interfaces, respectively, Y_w is the water cut，$S = \pi(R_2^2 - R_1^2)$ is the cross-sectional area of the fluid.

C_0 is a constant and its expression is

$$C_0 = \frac{2\pi\varepsilon\varepsilon_0 L}{\ln(R_5/R_4)} \tag{1}$$

The expression for C_{ew} is

$$C_{ew} = \frac{\beta\varepsilon\varepsilon_0 L}{\ln(R_3/R_2)} \tag{2}$$

The expression for C_{ewb} is

$$C_{ewb} = \frac{4\beta'\varepsilon\varepsilon_0 L}{\ln(R'/R_0)}(Y_w - Y_w^2) \tag{3}$$

Under the expression, $R' = \frac{1}{2}(R_1 + R_2)$, $\beta' = 2\alpha r \cos(R_1/R_2)$, C_{pw} is divided into three stages of expression as shown in Fig. 3(a), Fig. 3(b), and Fig. 3(c).

As shown in Fig. 3(a), when $\beta \leq 2\alpha r \cos(\frac{R_1}{R_2})$:

$$Y_w = \frac{(\beta - \sin\beta)R_2^2}{2S} \tag{4}$$

$$C_{pw} = 0 \tag{5}$$

$$C_{pwb} = \frac{\beta\varepsilon\varepsilon_0 L}{\ln(R''/R_0)} \tag{6}$$

Under the expression, $R'' = \frac{1}{2}(R_2 + R_2 \cos\frac{1}{2}\beta)$.

As shown in Fig. 3(b), when $2\pi - 2\alpha r \cos(R_1/R_2) \leq \beta \leq 2\alpha r \cos(R_1/R_2)$,

$$Y_\omega = \frac{\beta R_2^2 - \alpha R_1^2 - 2R_1 R_2 \sin[(\beta-\alpha)/2]}{2S} \tag{7}$$

$$C_{pw} = \frac{\alpha\varepsilon\varepsilon_0 L}{\ln(R_1/R_0)} \tag{8}$$

$$C_{pwb} = \frac{\beta\varepsilon\varepsilon_0 L(1 - \alpha/2\pi)}{\ln(R'/R_0)} \tag{9}$$

Under the expression, $\alpha = 2\alpha r \cos(\frac{R_2 \cos\frac{1}{2}\beta}{R_1})$.

As shown in Fig. 3(c), when $\beta \geq 2\pi - 2\alpha r \cos(R_1/R_2)$,

$$Y_w = \frac{\beta R_2^2 - 2\pi R_1^1 - R_2^2 \sin\beta}{2S} \tag{10}$$

$$C_{pw} = \frac{2\pi\varepsilon\varepsilon_0 L}{\ln(R_1/R_2)} \tag{11}$$

$$C_{pwb} = \frac{\beta\varepsilon\varepsilon_0 L(2\pi - \alpha)}{2\pi \ln(R'/R_0)} \tag{12}$$

Based on the theoretical analysis, the relationship between the output capacitance and the water cut can be determined as shown in Fig. 4.
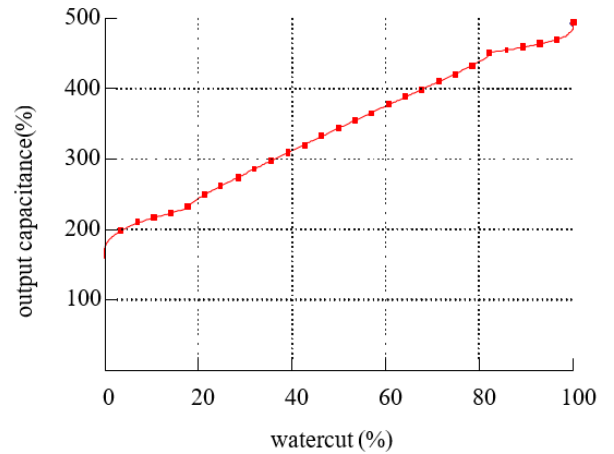

Fig. 4. The relationship between output capacitance and water cut.

3. EXPERIMENTAL MODEL

Numerical simulation is an effective means to study the flow pattern distribution characteristics of various structural horizontal pipes and provides technical support for the analysis of fluid flow patterns in the sensor flow pipeline and the optimization of the sensor structure. The new tri-electrode capacitive sensor uses an annular measuring pipeline to measure the water content. Its special structure cannot measure the real fluid flow pattern through dynamic experiments in the invisible pipeline. Therefore, we will calculate the flow pattern of the oil-water two-phase flow in the annular measurement pipeline at different inclination angles through numerical simulations as a technical support for the subsequent analysis of the dynamic experiment results. Fig. 5 shows the structural model of the annular measurement area of the new tri-electrode capacitive sensor.
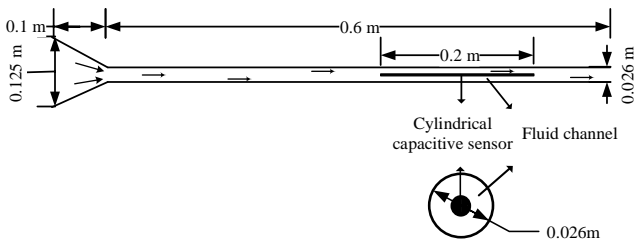

Fig. 5. Structure model of the annular measurement area of the new tri-electrode capacitive sensor.

The model consists of an isosceles trapezoidal structure with a length of 100 mm and a width that gradually tapers from 125 mm to 26 mm at the left end to simulate a flow-collecting umbrella. A horizontal straight pipe measuring 600 mm in length and 26 mm in width is connected to the right end of the collector umbrella model to mimic a new capacitive annular measurement pipeline. The front end of the straight horizontal pipe is a 300 mm long section with steady flow, and there is a coaxial center electrode in the middle of the horizontal straight pipe, which is 200 mm long and 3.8 mm wide. A two-dimensional axisymmetric simulation model is used in this paper. First, the annular measurement area modeled in the simulation is a symmetrical shape, so the results obtained with a two-dimensional model are consistent with those obtained with a three-dimensional model. In addition, the two-dimensional model simplifies calculations and storage, which improves the simulation efficiency. Finally, a two-dimensional model that focuses on the cross-sectional area can provide a more accurate description of the issue. The width of the center electrode of the sensor requires a conversion according to the fluid flow area of the actual annular flow pipeline, as shown in the equation:

$$\frac{S_1}{S_2} = \frac{D_1}{D_2 - D_1} \tag{13}$$

where S_1 and S_2 are the area of the electrode rod and the flow pipeline, respectively, and D_1 and D_2 are the diameter of the electrode rod and the combined capacitive sensor, respectively. Then we get the equation:

$$\frac{\Pi * 5^2}{\Pi * (13^2 - 5^2)} = \frac{D_1}{26 - D_1} \tag{14}$$

For the oil-water two-phase flow, the continuity equation of the oil-water two-phase flow without considering the energy conversion between the phases is expressed as follows:

$$\frac{\partial(\rho_o A_o)}{\partial t} + \frac{\partial(\rho_o A_o V_o)}{\partial x} = \tau_o A \tag{15}$$

$$\frac{\partial(\rho_w A_w)}{\partial t} + \frac{\partial(\rho_w A_w V_w)}{\partial x} = \tau_w A \tag{16}$$

where o and w denote the oil and water phases, respectively, ρ denotes the density, A denotes the cross-sectional area inside the oil-water two-phase flow tube, t denotes the time, V denotes the average velocity, and τ_o, τ_w are the source terms of the mass produced per unit of time in the tube. When a fluid is produced, τ_o is positive, according to the law of conservation of mass $\tau_o = -\tau_w$.

The momentum squares for the oil and water phases are, respectively:

$$\frac{\partial(\rho_o A_o v_o)}{\partial t} + \frac{\partial(\rho_o A_o v_o^2)}{\partial x} - \tau_o A \hat{v} = -\tau_o S_o +$$
$$+ \tau_1 S_1 - \rho_o g A_o \sin\beta - \frac{\partial(\rho_o A_o)}{\partial x} + P_{Io} \frac{\partial A_o}{\partial x} \tag{17}$$

$$\frac{\partial(\rho_w A_w v_w)}{\partial t} + \frac{\partial(\rho_w A_w v_w^2)}{\partial x} - \tau_w A \hat{v} = -\tau_w S_w +$$
$$+ \tau_1 S_1 - \rho_w g A_w \sin\beta - \frac{\partial(\rho_w A_w)}{\partial x} + P_{Iw} \frac{\partial A_w}{\partial x} \tag{18}$$

where I is the interface, β is the angle between the pipe and the horizontal direction and S is the interface length.

When $\tau_w > 0$, $\hat{v} = v_o$, when $\tau_w > 0$, $\hat{v} = v_w$.

When creating a 2D simulation model for a new capacitance sensor, the center electrode does not allow the fluid to flow up and down in the section, which makes the simulation results inconsistent with the real flow pattern. To solve this problem, this paper proposes to make 20 slits of 1 mm width at equal intervals on the center electrode so that the fluid can bypass it. Fig. 6 depicts the two-dimensional simulation model of the annular measurement area of the new tri-electrode capacitive sensor at an inclination angle of 0°. Triangular meshes were used for the experiment, and the grid was divided into 125,303 elements. Firstly, triangular meshes are better suited for areas with curvatures or complex structures, such as pipelines. Secondly, they provide better mesh quality, especially for sharp geometric features or situations that require finer mesh partitioning. Finally, triangular meshes can provide higher computational efficiency.

Fig. 6. Two-dimensional simulation model of the annular measurement area of the new tri-electrode capacitive sensor.

The inlet is set as a velocity inlet, while the outlet is defined as an outflow. The walls of the pipeline are referred to as solid boundaries. Linear triangular elements are used for the simulation. The linear triangular elements that are used for the simulation can fulfill the Babuska-Brezzi condition. The materials are oil and water and the parameters are shown in Table 1.

Table 1. Fluid parameters.

Parameters	Density [kg/m^3]	Viscosity [kg/(m·s)]	Surface tension [N/m]
oil	850	0.0103	0.019
water	998	0.0010	——

The visible experimental device for studying the measurement pipeline of the capacitive sensor consists of a transparent Plexiglas pipe as the main body, and the horizontal inclination of the experimental well section can be adjusted between 0° and 90° with an accuracy of 0.1°, as shown in Fig. 7. Before the fluid enters the experimental section of the visible DN20 pipe, tit passed through a DN125 flow pipe. The purpose is to simulate the real working conditions of a downhole fluid flowing through a collection umbrella and then into a measurement pipeline, which makes it possible to study the change in the flow pattern after the diameter reduction through the collection umbrella. The test medium was D110 white oil and water. During the experiment, the change of the flow pattern of the oil-water two-phase flow was observed with a high-speed camera in the range of 0-5° horizontal inclination angle, 1-60 m^3/d flow rate, and 20-90% water content.

Fig. 7. A DN20 simulator for measuring the pipeline of the capacitive sensor.

In this section, the simulation and experimental study of the flow pattern of the near-horizontal oil-water two-phase flow of the sensor measurement pipeline is carried out to understand the flow patterns of the oil-water two-phase flow in the DN20 pipeline and to provide technical support for the analysis of the subsequent dynamic experiment and the optimization design of the sensor. For the theoretical simulation analysis, the fluid mechanics simulation software FLUENT is used, which simulates and reproduces the complex flow of multi-phase fluid on the computer using a partial differential algorithm, which effectively controls the time and cost of the study and improves the efficiency of the work. The geometric model structure of the DN20 test device was created as shown in Fig. 8.

The left end of the model has an inner diameter of 125 mm and a length of 0.5 m. The horizontal borehole model and the right side of the horizontal borehole are connected with an isosceles trapezoidal transition section with a length of 50 mm and a width reduced from 125 mm to 20 mm, which is used to simulate the flow collection umbrella. A flow collection pipeline model with a diameter of 20 mm and a length of 1 m is connected to the right of the umbrella.
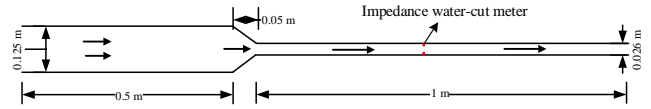

Fig. 8. Geometric model structure of the DN20 experimental device.

Fig. 9 shows the grid model created by the geometric structure using the triangular form of the element division, the number of divided grids is 145704. Setting its boundary conditions: velocity_inlet on the left side, outflow on the right side, internal fluid, two horizontal inclination angle grid models were created for the DN20 experimental device with 0° and 5°. At the same time, a dynamic experimental study of the oil-water two-phase flow under different horizontal inclination angles, flow rates and water contents in the DN20 experimental device was conducted, and the oil-water two-phase flow pattern under each working condition was recorded by a high-speed camera located 20 cm behind the collector inlet of the device.
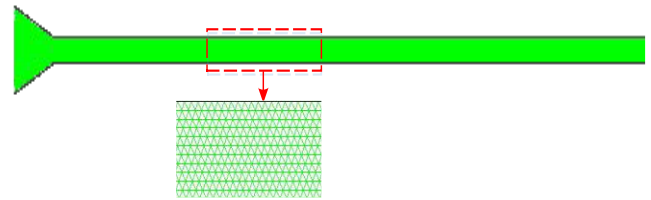

Fig. 9. Schematic diagram of mesh generation of the DN20 experimental device.

4. THE THEORETICAL AND EXPERIMENTAL COMPARISON

A. DN20 horizontal pipe

A significant amount of fundamental research has been carried out worldwide on horizontal oil/water two-phase pipe flow under various conditions. The primary flow patterns are shown in Fig. 10.

Fig. 11 shows the simulation and experimental results for the same horizontal conditions, both with 50% water content and different flow rates. The fluid in the measurement pipeline exhibits a smooth, stratified flow at flow rates of 5 m^3/d and 10 m^3/d. The oil-water interface is consistent at a water content of 50%, with slight fluctuations as the flow rate increases. At a flow rate of 30 m^3/d, the fluid exhibits a water-in-oil and a water-laminar flow. Due to the high flow rate, the upper oil layer experiences increased fluctuations. These strong fluctuations cause part of the oil phase to separate from the continuous oil phase and form large oil droplets that float in the lower water phase. However, as the measurement pipeline length increases, the fluid gradually tends towards the laminar flow type, indicating that the flow pattern

stabilizes along the path of the measurement pipeline if it is long enough. At a flow rate of 60 m³/d, the high-speed fluid mixed the two phases of oil and water well, creating a fine-bubble flow type of water-in-oil and oil-in-water.
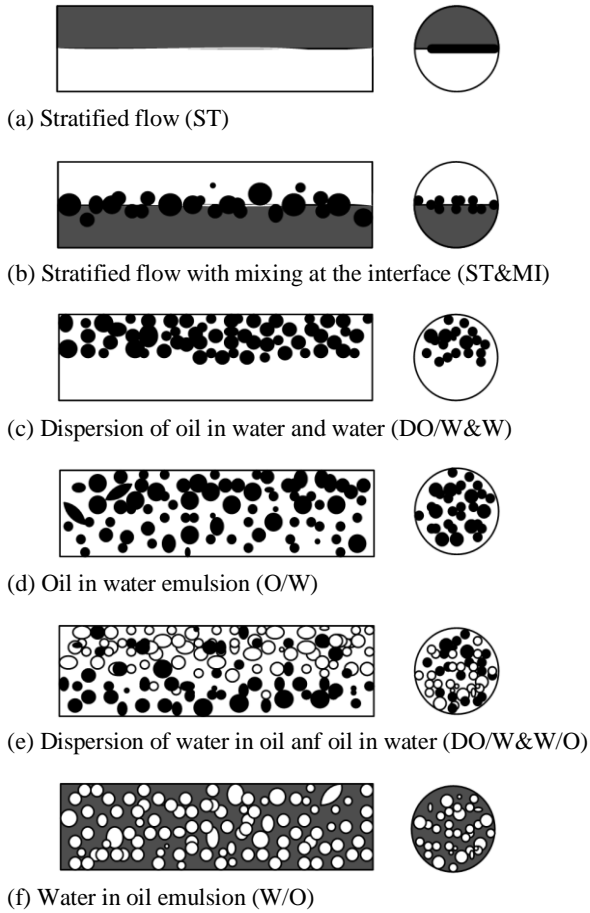

(a) Stratified flow (ST)

(b) Stratified flow with mixing at the interface (ST&MI)

(c) Dispersion of oil in water and water (DO/W&W)

(d) Oil in water emulsion (O/W)

(e) Dispersion of water in oil anf oil in water (DO/W&W/O)

(f) Water in oil emulsion (W/O)

Fig. 10. Classification of flow patterns of the oil-water two-phase flow in a horizontal pipe.
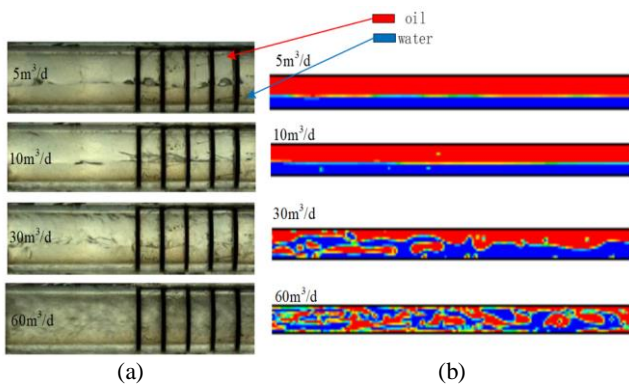

(a)   (b)

Fig. 11. The simulation results and dynamic experimental results of the oil-water flow pattern of the DN20 visible experimental device at 50% water content and 0°: (a) Simulation results, (b) Dynamic experimental results.

The experimental results showed that the oil and water phases in the measurement pipeline exhibited a smooth, stratified flow at low flow rates (5 m³/d and 10 m³/d). The oil-water interface showed slight fluctuations, which increased with increasing flow rate. At a flow rate of 30 m³/d, the fluid

tends towards the turbulent flow type and the upper oil layer shows significant oscillations. The fast-flowing oil layer moves from the top towards the center of the measurement pipeline. Despite the dispersion of some oil bubbles into the water layer at the bottom, the oil layer remains continuous. At a flow rate of 60 m³/d, the fluid tends towards the turbulent flow type. The two phases of oil and water in the measurement pipeline are well mixed and merge into a fine bubble flow with a thin layer of water at the bottom.

Fig. 12 shows the simulation and experimental results under horizontal conditions, a water content of 70% and different flow rates.

The oil-water two-phase flow becomes a smooth, stratified flow within 10 m³/d at a low flow rate, and the height of the oil-water interface is higher than the height of the liquid surface at 50% water content. The oil layer in the upper part of the measurement pipeline fluctuates more drastically at 30 m³/d, and the size of the oil droplets drifts freely in the water layer. The length of the steady-pattern laminar flow is shorter when the water content is below 50%. This phenomenon indicates that at an average flow rate of 30 m³/d, the length of the measurement pipeline of the fluid tending to the steady state of laminar flow is related to the flow rate and water content. At a flow rate of 60 m³/d, oil and water are evenly mixed. As the water content increases, most of the borehole consists of the water phase, which becomes a water-covered fine oil bubble-like flow pattern, and the oil phase becomes fine oil bubble-like in the upper part of the measurement pipeline. The dynamic experimental results agree with the simulation results.

The dynamic experiments show that at low flow rates of less than 10 m³/d, the oil and water phase in the measurement pipeline becomes a smooth, stratified flow. The height of the oil-water interface increases due to the increased water content. When the flow rate increases to 30 m³/d, the fluid tends towards the turbulent flow type and the fluctuation of the oil layer increases. The turbulent pattern of the oil layer in the upper part of the measurement pipeline can be observed due to the increasing flow rate, and there are oil bubbles that break away from the continuous oil phase and float freely in the water. When the flow rate reaches 60 m³/d, complete mixing of oil and water occurs. The buoyancy of the water causes the dispersion of the fine oil bubbles to become more concentrated at the top, resulting in a thinner water layer at the bottom.

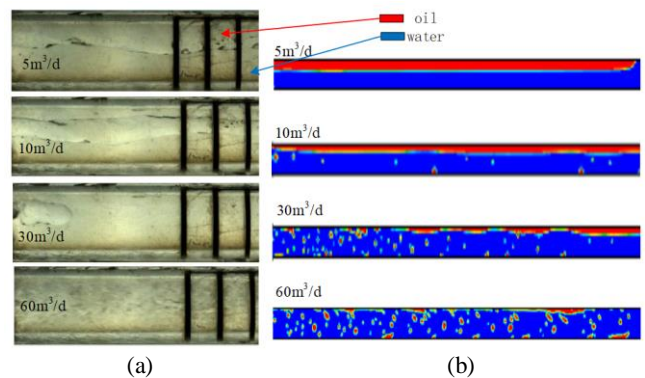(a)   (b)

Fig. 12. The simulation results and dynamic experimental results of the oil-water flow pattern of the DN20 visible experimental device at 70% water content and 0°: (a) Simulation results, (b) Dynamic experimental results.

Fig. 13 illustrates the simulation and experimental results for horizontal conditions, especially with 90% water content and different flow rates.

From the simulation results in Fig. 10, it can be seen that the oil and water phase in the measurement pipeline becomes a smooth, stratified flow at a flow rate of 5 m^3/d. At a flow rate of 10 m^3/d, the oil layer in the upper part of the flume becomes thin and there are only a few free oil bubbles in the water phase. At the medium flow rate of 30 m^3/d, the oil phase flows discontinuously into the water phase and changes the flow type to oil-in-water, with longer oil globules at the top of the measurement pipeline and fine oil bubbles in the middle of the pipe. As the pipe lengthens, the fine oil bubble in the center decreases and the oil phase changes to large discontinuous oil globules at the top of the pipe. At a flow rate of 60 m^3/d, there is a uniform fine oil bubble in the water flow pattern in the measurement pipeline.

The dynamic experimental results agree with the simulation results. At a flow rate of 5 m^3/d, the oil and water phase in the measurement pipeline becomes a smooth, stratified flow, and the fluctuation of the oil-water interface shows minimal fluctuations. At a flow rate of 10 m^3/d, the borehole is occupied by the water phase due to the high-water content. The oil phase leaves the top of the measurement pipeline and is free in the water as a continuous thin layer of oil. At a flow rate of 30 m^3/d, the water phase flow rate increases so that the oil phase cannot maintain the continuous phase pattern. The oil phase transports the continuous water phase in the form of non-continuous large oil globules. At a flow rate of 60 m^3/d, the oil phase becomes fine oil droplets. The water flow pattern in the measurement pipeline contains fine oil bubbles.
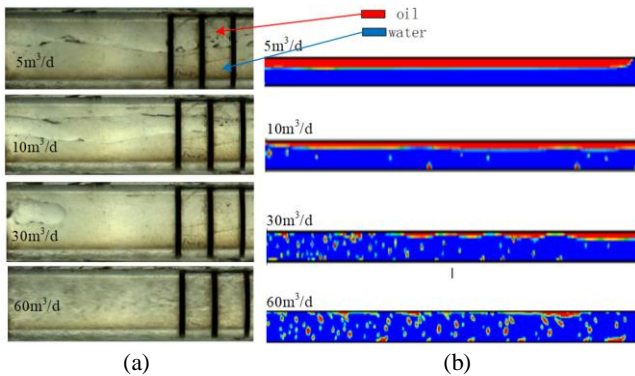

Fig. 13. The simulation results and dynamic experimental results of the oil-water flow pattern of the DN20 visible experimental device at 90% water content and 0°: (a) Simulation results, (b) Dynamic experimental results.

Similar flow laws are observed at various water rates, e.g. at 50%, 70%, and 90% water content under horizontal conditions. When the fluid flow rate is below 10 m^3/d, it takes on a smooth, stratified flow pattern. At the 30 m^3/d medium flow rate, the oil flow pattern tends to change to a non-continuous sphere. At the high flow rate of 60 m^3/d, the flow pattern is a fine oil bubble in the water and oil and water are completely mixed.

B. Different inclination DN20 horizontal pipe

Fig. 14 shows the simulation and experimental results at a horizontal inclination angle of 5°, a water content of 50% and different flow rates.

At a flow rate of 5 m^3/d and 10 m^3/d, oil and water in the measurement pipeline become a smooth, stratified flow. Due to the effect of flow collection and acceleration achieved by the small diameter of the pipe, the oil-water interface runs parallel to the pipe. At 30 m^3/d, the upper part of the measurement pipeline is a turbulent continuous oil phase. Some oil droplets detach from the continuous oil phase and are released into the water phase. If the fluid continues to flow in the extended measurement pipe section, the oil and water phases gradually tend towards the laminar flow type. At 60 m^3/d, oil and water are evenly mixed. A fine oil-in-water and water-in-oil flow pattern can be seen in the measurement pipe. Influenced by the inclination angle, the evenly mixed and high-speed oil-water two-phase flow flows in the middle and upper part and a thin water layer at the bottom of the measurement pipeline.

The dynamic experimental results agree with the simulation results: at low flow rates within 10 m^3/d, the oil and water phases in the measurement pipeline become a smooth, stratified flow, the amplitude of the fluctuation increases with the flow rate, the height of the oil-water surface parallel to the measurement pipeline is lower than under horizontal conditions. At 30 m^3/d, the upper oil layer fluctuates dramatically. Some oil bubbles are separated from the oil layer and released into the water layer. At a horizontal inclination angle of 5°, it becomes clear that there is a separation between oil and water. The flow rate of the oil phase is higher than that of the water phase due to gravity. At a flow rate of 60 m^3/d, the two-phase mixing of oil and water in the borehole is sufficient, and the measurement pipeline is full of high-speed flow of tiny oil bubbles, showing a fine oil bubble-like flow pattern. Since the flow velocity in the collection measurement pipeline is almost 40 times higher than in the horizontal borehole, changing the horizontal inclination angle within 5° has little effect on the flow pattern in the collection measurement pipeline.
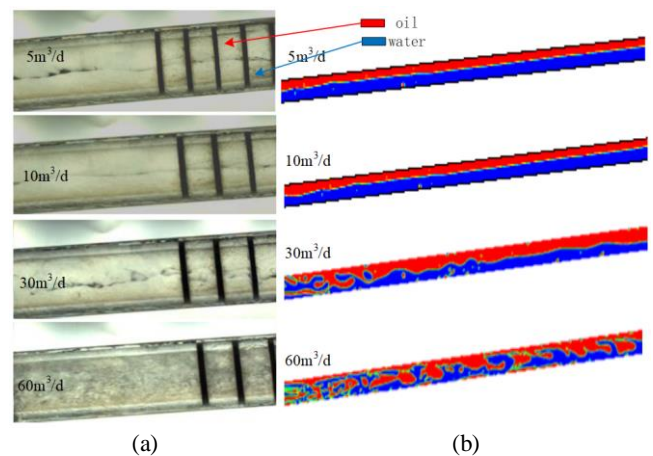

Fig. 14. The simulation results and dynamic experimental results of the oil-water flow pattern of the DN20 visible experimental device at 50% water content and 5°: (a) Simulation results, (b) Dynamic experimental results.

Fig. 15 shows the simulation and experimental results at a horizontal inclination angle of 5°, a water content of 70% and different flow rates.

The experimental results of the flow rate at 70% water content are similar to those at 50% water content, so the flow pattern analysis is not repeated here. However, the oil-water surface area increases due to the higher water content. In addition, the simulation results show that the bubble diameter of the oil bubbles free in the water is smaller at a water content of 70% than at a water content of 50% at medium and high flow rates.

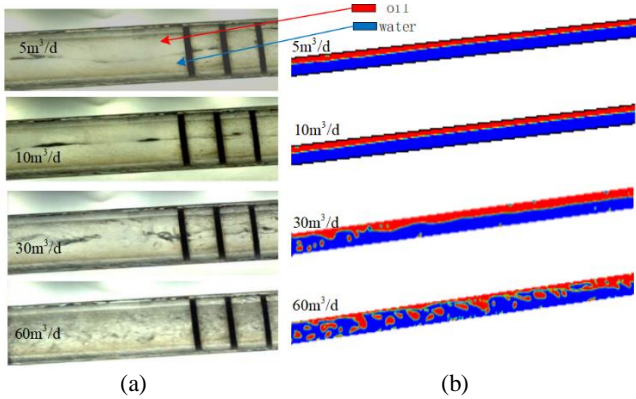(a)   (b)

Fig. 15. The simulation results and dynamic experimental results of the oil-water flow pattern of the DN20 visible experimental device at 70% water content and 5°: (a) Simulation results, (b) Dynamic experimental results.

Fig. 16 shows the simulation and experimental results at a horizontal inclination angle of 5°, a water content of 90% and different flow rates.

The results of the simulation and the dynamic experiments are consistent. At low flow rates within 10 m³/d, the oil and water phase in the measurement pipeline is still a smooth, stratified flow, and the oil-water surface height increases with increasing water content. At a flow rate of 30 m³/d, the fluid in the measurement pipeline changes to an oil-in-water flow. The oil phase consists mainly of large droplets that move discontinuously along the top, with a few small droplets in the center. At a flow rate of 60 m³/d, the oil-water mixture is sufficient and shows a fine oil bubble-like flow pattern.

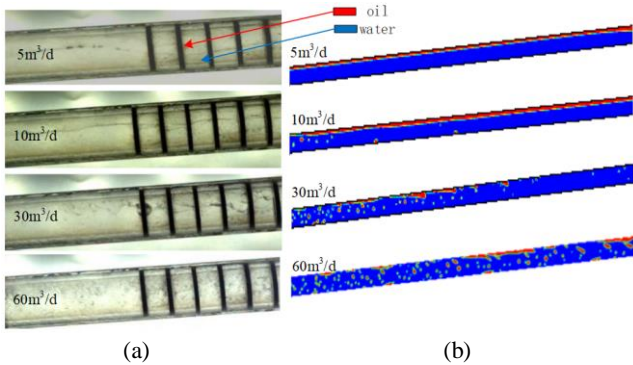(a)   (b)

Fig. 16. The simulation results and dynamic experimental results of the oil-water flow pattern of the DN20 visible experimental device at 90% water content and 5°: (a) Simulation results, (b) Dynamic experimental results.

From the above analysis, it can be concluded that the horizontal inclination angle has little influence on the flow pattern. This is because the fluid flow rate in the DN20 measurement pipeline is 40 times higher than in the DN125 measurement pipeline.

5. NUMERICAL APPROACH

The DN20 fluid simulation model was validated through dynamic experiments and simulation analyses. This model is then used to observe the flow characteristics of the oil-water two-phase flow in an invisible flow pipeline under different working conditions. This observation helps to interpret the subsequent dynamic experimental data. Three grid models with horizontal inclination angles of 0°, -5°, and 5° are created to study the characteristics of the oil-water two-phase flow at different flow rates and water contents.

A. Invisible horizontal pipe

If you set the horizontal inclination angle to 0°, the oil-water flow rate to 10 m³/d, 30 m³/d, and 60 m³/d and the water content to 30%, 50%, and 90%, respectively, the simulation results of the oil-water two-phase flow type in the new capacitive sensor measurement pipeline are shown in Fig. 17.
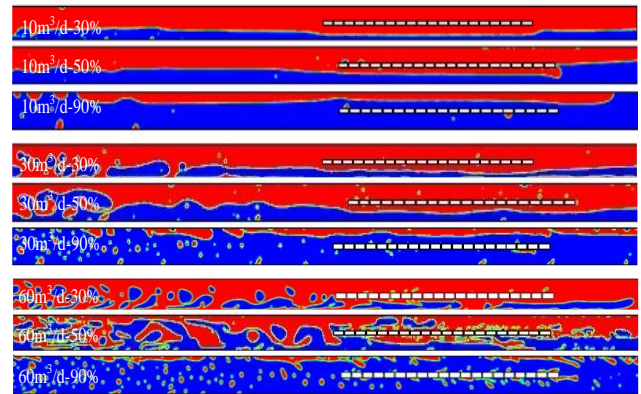

Fig. 17. The flow pattern of the new capacitive water content sensor measuring pipelines under different working conditions when the horizontal inclination angle is 0°.

The flow pattern in the measurement pipeline at a flow rate of 10 m³/d under different water content conditions shows a smooth, stratified flow. At a water content of 30% and 50%, the oil phase floods the center electrode, reducing the flow space. This causes stagnation of the oil phase around the center electrode, resulting in a lower oil surface level. As a result, the sensor response is lower than the actual water content. On the other hand, when the water content reaches 90%, the center electrode is immersed in the water phase. In this situation, the metal layer electrode primarily measures the dielectric properties of the upper oil layer. Due to the shielding effect of the water phase on the center electrode, the sensor output exceeds the actual water content, preventing the detection of oil and water. At an oil-water flow rate of 30 m³/d and a water content of 30% and 50%, the sensor's measuring pipeline exhibits a stratified flow pattern characterized by wave-like formations. The center electrode

and the metal layer electrode, which are immersed in the oil phase, accurately measure the dielectric properties of the upper continuous oil phase. This results in a higher sensor resolution and a response that is closer to the actual water-holding capacity. However, at a water content of 90%, the submerged water phase shields the rod electrode so that it can no longer measure effectively. As a result, the cylindrical electrode primarily measures the dielectric properties of the top layer of oil, resulting in a higher sensor response than the actual water-holding capacity.

At a flow rate of 60 m³/d and a water content of 30%, the fluid in the measurement pipeline is of the water-in-oil type. The water phase is carried through the center of the measurement pipeline and appears as large water droplets. When these droplets pass near the center electrode, they turn into a discontinuous slug flow. In this scenario, the metal layer electrode and the center electrode of the sensor are surrounded by a continuous oil phase in the measurement area. As a result, the sensor has an improved resolution. However, due to the high-speed flow of the non-continuous water phase in the center of the pipeline, some water may come into contact with the center electrode, leading to a slightly higher response value than the actual water content. At 50% water content, the flow type is water-in-oil and water layer. There is a continuous oil phase with water droplets flowing in the middle and upper part of the measurement pipeline while the water layer flows in the bottom region. The upper part of the metal layer electrode and the center electrode are both surrounded by the continuous oil phase, while the lower water layer surrounds the remaining two electrodes. The response value of the sensor, which is influenced by such a flow pattern, is higher than the actual water content. At a water content of 90%, the flow pattern resembles fine oil bubbles dispersed in water. The center and the metal layer electrode are wrapped and shielded by the water phase. As a result, the resolution of the sensor is reduced, and its response values approach those observed when the sensor is fully immersed in water. To summarize, the new capacitive sensor is not suitable for measuring high flow rates and the oil-water two-phase flow with high water content.

B. The positive angle horizontal pipe

If you set the horizontal inclination angle as +5°, the flow rate as 10 m³/d, 30 m³/d, and 60 m³/d and the water content as 30%, 50%, and 90%, respectively, the simulation results of the oil and water two-phase flow type in the new capacitive sensor measurement pipeline are shown in Fig. 18.

The horizontal inclination induces an oil-water slip, resulting in a notable increase in the water phase proportion in the horizontal pipe. At a total flow rate of 10 m³/d and a water content of 30%, the oil phase is sufficient to flood the center electrode so that both the center electrode and the metal layer electrode can measure the dielectric properties of the oil. At a water content of 50%, part of the center electrode is flooded by the water phase, which can limit part of its measurement capacity. As a result, the sensor resolution capacity is reduced. At a water content of 90%, the oil phase flows in the form of discontinuous thin oil droplets along the upper part of the inner wall of the measurement pipeline. The

center electrode, which is immersed in water, has no resolution, and the sensor response value tends to correspond to the full water value. At a total flow rate of 30 m³/d and a water content of 30-50%, the flow pattern is laminar flow and the center electrode immersed in the oil phase has a high resolution. At a water content of 90%, the center electrode loses its differentiation ability when it is immersed in the water phase. The metal layer electrode can make contact with and measure the dielectric properties of the discontinuous oil layers above. As a result, the sensor has a high response value that approaches the value observed when the sensor is fully immersed in water.
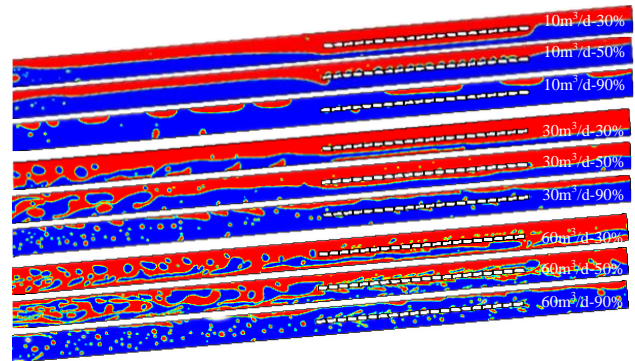

Fig. 18. The flow pattern of the new capacitive water content sensor measuring pipelines under different working conditions when the horizontal inclination angle is +5°.

With a total flow rate of 60 m³/d and a water content of 30%, the flow pattern is bubble-like water in continuous oil. The oil phase surrounds the center electrode and part of the metal layer electrode, resulting in a high sensor resolution and a response value that is very close to the actual water-holding value. When the water content reaches 50%, the top layer of oil becomes less thick. In the middle, the water flow pattern resembles the bubbles in the oil. There is a consistent layer of water at the bottom of the measurement pipeline. As the lower water phase shields part of the metal layer electrode, the sensor response value is higher than the actual water-holding rate: at a water content of 90%, the oil phase flows in the upper region of the measurement pipeline in the form of fine bubbles. The water phase shields both the center electrode and part of the metal layer electrodes, causing the sensor response value to approach the measured value at full water saturation.

C. The negative angle horizontal pipe

If you set the horizontal inclination angle as -5°, the total flow rate as 10 m³/d, 30 m³/d, and 60 m³/d and the water content as 30%, 50%, and 90%, respectively, then the simulation results of the oil-water two-phase flow type in the new capacitive sensor measurement pipeline are shown in Fig. 19.

The simulation results indicate a notable oil-water slip effect, where the buoyancy of the water phase traps the oil phase inside the measurement pipeline at a flow rate of 10 m³/d. At a water content of 30% or 50%, a stratified flow occurs in the measurement pipeline. Most of the measurement pipeline is occupied by the oil phase with only a thin,

continuous layer of water at the bottom, so the response of the sensor tends to be the full oil value. When the water content is 90%, the trapped oil phase floods the upper part of the center electrode. This results in a biased response value towards a lower oil phase value compared to the condition at horizontal and positive inclination angles. At a total flow rate of 30 m³/d, the oil phase is slowed down by the buoyancy of the water. Under the same operating conditions, the proportion of the oil phase in the measurement pipeline exceeds that of the oil phase at horizontal and forward inclination. At a water content of 30% or 50%, the fluid in the measurement pipeline is a stratified oil-water flow with a thin water layer at the bottom. The new capacitive sensor is wrapped mostly by the oil phase and has a high resolution. At a water content of 90%, the oil phase forms a non-continuous thin layer in the upper part of the pipeline. The center electrode, which is immersed in the water phase, loses its discrimination ability. In contrast, the metal layer electrode can measure the dielectric properties of the oil layer it comes into contact with. As a result, the sensor response value approaches the value corresponding to full water.
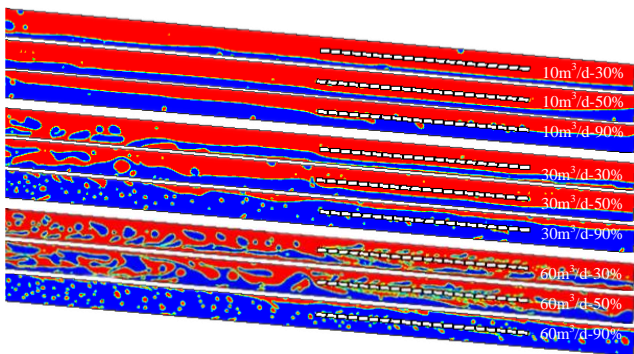

Fig. 19. The flow pattern of the new capacitive water content sensor measuring pipelines under different working conditions when the horizontal inclination angle is -5°.

At a total flow rate of 60 m³/d and a water content of 30%, the flow pattern observed in the measurement pipeline is a water-in-oil pattern. The water phase flows within the continuous oil phase and appears as fine bubble-like water droplets near the center electrode or as thin and discontinuous water layers at the bottom of the center electrode. As a result, both the center electrode and the metal layer electrode have good resolution capabilities. At a water content of 50%, the water phase flows as a continuous water layer at the bottom of the center electrode or as non-continuous water bubbles in the middle of the pipeline. The water phase covering part of the metal layer electrode slightly affects the resolution. When the water content reaches 90%, the oil phase flows as a thin layer at the top of the measurement pipeline or in the form of sporadic oil bubbles near the center electrode, which comes into contact with part of the metal layer electrode. As a result, the resolution ability is reduced, and the response value approaches the value corresponding to full water.

To summarize, the new capacitive sensor can be used for a variety of flow types, such as laminar and bubble flow types. When the flow type is laminar at the low total flow rate, the sensor can measure the oil-water two-phase flow at a water

content of 0 to 100%. However, the response value of the sensor is affected by the horizontal inclination angle, resulting in a bias towards the oil phase value at a positive horizontal angle or a bias towards the water phase value at a negative horizontal angle. If the flow type is a fine bubble flow with a high total flow rate, the sensor has a higher measurement resolution in a water content of 0-50%. The response value is close to the actual water-holding rate and the effect of the horizontal inclination angle is lower. However, the sensor resolution decreases at high water content due to the shielding effect of the water.

6. NEW SENSOR SYSTEM

Fig. 20 shows the working principle of the new capacitive water content sensor under horizontal conditions. The metal layer electrode and the center electrode are connected in parallel in the circuit of the new capacitive sensor, which is jointly sensitive to the change in the water content in the measurement pipeline. The capacitance Cx generated by the new capacitive sensor is used to modify the output of the frequency oscillator circuit. The output frequency of the measurement system is $F = k/Cx$, where k is the proportionality constant. The moisture content can be measured by measuring the output frequency of the instrument.
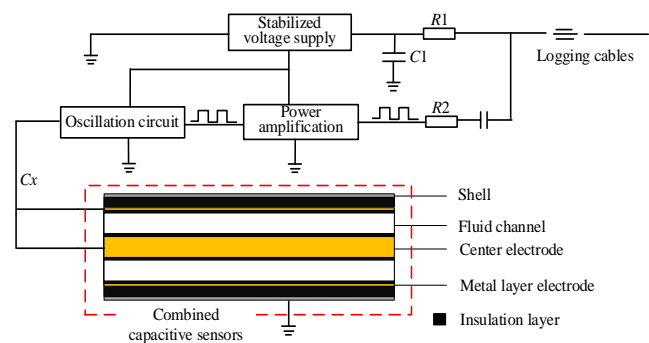

Fig. 20. Schematic diagram of the operation of the new capacitive sensor.
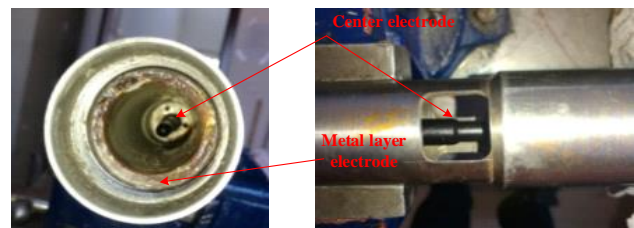

Fig. 21. Structure and prototype of the combined capacitance sensor.

The tri-electrode capacitive sensor shown in Fig. 21 consists of a center electrode, a cylindrical metal layer electrode, and an outer shell. The inner and outer layers of the cylindrical metal layer electrode are wrapped with insulating material and only one wire, which is insulated from the outer shell, is led out. Similarly, the center electrode is also wrapped with insulating heat-shrinkable tubing and only one wire, which is insulated from the outer shell, is led out at the

root of the electrode. These two wires are connected to an excitation power source. This connection arrangement can be compared to two capacitors connected in parallel. The capacitance value of this configuration varies with changes in water or moisture content.

Fig. 22 shows a flow-water cut combined logging tool consis ing mainly of a flow collector, a flowmeter, a water cut meter, and supporting electrical systems. This instrument uses flow collection techniques to perform targeted tests of flow rates and water cuts at various measurement intervals. The water cut meter uses a tri-electrode capacitive water cut sensor, while the flowmeter is a turbine flowmeter.

Fig. 22. Flow and water cut measurement jointer of the horizontal well combiner.

7. DYNAMIC TESTS AND ANALYSIS

In this section, a dynamic experimental study of the new capacitive sensor is carried out. Fig. 23 shows the dynamic simulation experimental well, while Fig. 24 presents the new capacitive logging instrument. The instrument is placed in the test well, which can simulate a real oil-water two-phase flow, to investigate its ability to measure water content. In the experiment, the range of flow rates is 3 m³/d to 30 m³/d, and the range of water content is 10% to 100%. The output frequency of the new capacitive logging instrument is recorded at each fixed flow rate and water content. Then the output frequency values of the new capacitive sensor are normalized. The normalization method is: the frequency value f corresponding to each flow rate and water content is substituted into the formula to obtain the normalized response Y

$$Y = \frac{|f - f_{\max}|}{f_{\max} - f_{\min}}$$, the range of Y is between 0 and 1,

and finally the relationship diagram between Y, flow rate and water content is established. The relationship between the normalized response of the new capacitive sensor and the variation of water content and flow rates is shown in Fig. 20, at horizontal inclination angles of 0°, -5°, and 5°.

Fig. 23. The dynamically simulated experimental well.

Fig. 24. The new capacitive logging instrument.
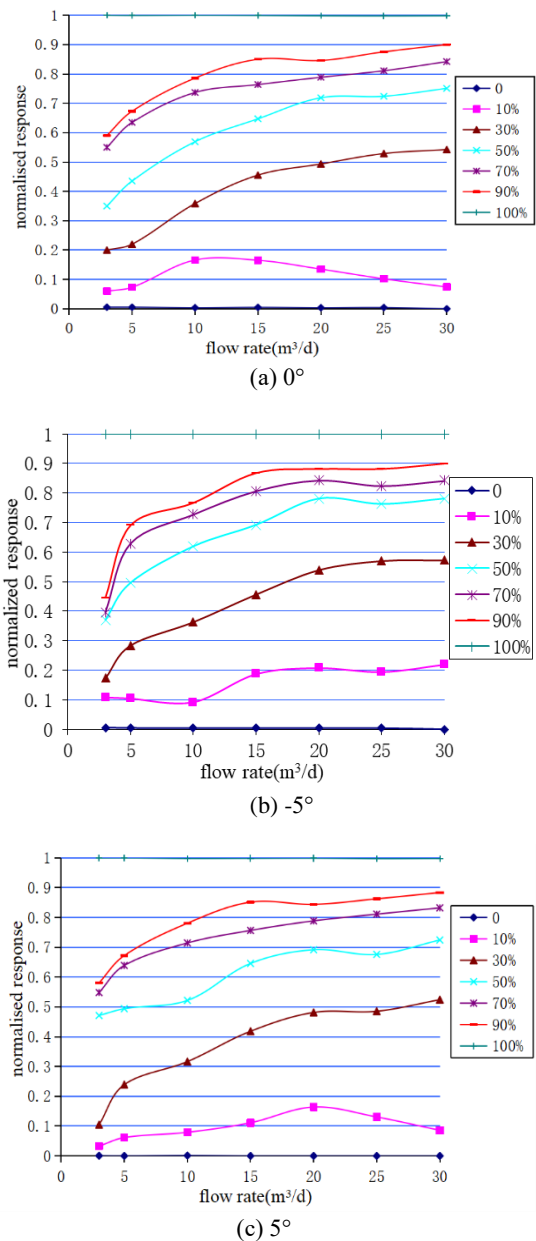

(a) 0°

(b) -5°

(c) 5°

Fig. 25. Response of the new capacitive sensor to changes in water content and flow rate at 0°, -5° and 5°.

Fig. 25(a) shows that the new capacitive sensor has accurate response characteristics at a flow rate of 3 m^3/d~30 m^3/d and a water content of 0-100% at a horizontal inclination of 0°. The interval between the curves at 70-100% water content is smaller than at 0-50% water content, indicating that the sensor has better resolution at low water content. At flow rates of less than 5 m^3/d, the curves converge towards the response value for low water content. This happens because the center electrode, which is more important for the measurement, is immersed in the continuous oil phase. However, the metal layer electrode is in contact with the bottom water phase. The layer of continuous oil covering the central electrode has the same thickness as the thickened center electrode insulation layer. Therefore, the response value of the instrument tends to be close to the full oil value. If you increase the flow rate from 15 m^3/d to 30 m^3/d, the gap between the curves increases, indicating that the response resolution of the sensor has increased proportionally. Since the flow pattern is a bubble-like oil-water two-phase flow at high flow rates, the frequency with which the oil bubble contacts the center electrode and the metal layer electrode is directly determined by the velocity and water content. Changes in the flow rate or water content have a direct effect on the sensor response. The curve patterns of the three graphs show similarities at flow rates from 15 m^3/d to 30 m^3/d and different horizontal inclination angles, as shown in Fig. 25(b) and Fig. 25(c). This is because the horizontal inclination has less influence on the flow pattern of the oil-water two-phase flow at higher flow rates under different water content conditions. The difference lies in the impact of the horizontal angle on the response character at a low flow rate, with the curves generally rising at 5° and falling at -5°. This difference is due to the higher oil phase at -5°C and the lower one at 5°C.

The dynamic experimental results show that the water content measurement range of the new capacitance sensor can reach 0~100% in 3 m^3/d~30 m^3/d under near-horizontal conditions. Therefore, the new capacitance sensor is more suitable for testing horizontal wells. However, the sensor has low resolution at high water content due to the electrode shielding by the water phase, so the response value approaches the low water content response value.

8. CONCLUSION

This paper uses a combination of numerical simulations and dynamic experiments to model and experimentally investigate the flow behavior of the oil-water two-phase flow in the DN20 visible glass pipeline under near-horizontal conditions. The study then simulated the flow pattern of the oil-water two-phase flow in the annular, non-visible measurement pipeline of the new capacitive sensor. The study also investigated the distribution characteristics of the oil-water two-phase flow in the sensor's measurement pipeline under different horizontal angles, flow rates, and water contents. A dynamic experiment was conducted to determine the sensor's responses at different horizontal inclination angles, flow rates, and water contents. The influence of the flow pattern on the sensor response under different working conditions was analyzed by numerical and experimental studies. The study concludes that the new capacitance sensor is suitable for measuring oil-water two-phase fluids at high

flow rates and medium to low water content. In addition, the change in the flow pattern is hardly affected by the horizontal inclination angle. This sensor can measure the oil-water two-phase fluids with a water content of 0% to 100% at low flow rates. Moreover, with a positive horizontal inclination angle, the sensor response value is biased towards a high water content. Conversely, a negative horizontal inclination angle will result in a biased response towards a low water content.

REFERENCES

[1] Xu, H. L., Jiang, H. S., Wang, J., Wang, T., Zhang, L. J. (2023). Formulation optimization of materials used in temporary plugging diversion between fracture front end and cluster in shale gas: From laboratory research to field application. *Physics of Fluids*, 35 (6), 063310. https://doi.org/10.1063/5.0151878

[2] Kong, W. H., Kong, L. F., Li, L., Liu, X. B., Xie, R. H., Li, J., Tang H. T. (2016). The finite element analysis for a mini-conductance probe in horizontal oil-water two-phase flow. *Sensors*, 16 (9), 1352. https://doi.org/10.3390/s16091352

[3] de Oliveira, M. R., Martins, M. F., Belich, H., Amorim, L. (2022). A model for predicting two-phase flow patterns transition in an annulus: Inclinations from horizontal to near-vertical. *Chemical Engineering Science*, 250 (15), 117379. https://doi.org/10.1016/j.ces.2021.117379

[4] Barnea, D., Shoham, O., Taitel, Y., Dukler, A. E. (1980). Flow pattern transition for gas-liquid flow in horizontal and inclined pipes: Comparison of experimental data with theory. *International Journal of Multiphase Flow*, 6 (3), 217-225. https://doi.org/10.1016/0301-9322(80)90012-9

[5] Mukherjee, H., Brill, J. P., Beggs, H. D. (1981). Experimental study of oil-water flow in inclined pipes. *Journal of Energy Resources Technology*, 103 (1), 56-66. https://doi.org/10.1115/1.3230815

[6] Trallero, J. L., Sarica, C., Brill, J. P. (1997). A study of oil-water flow patterns in horizontal pipes. *SPE Production and Operations*, 12 (3), 165-172. https://doi.org/10.2118/36609-PA

[7] Charles, M. E., Govier, G. W., Hodgson, G. W. (1961). The horizontal pipeline flow of equal density oil-water mixtures. *The Canadian Journal of Chemical Engineering*, 39 (1), 27-36. https://doi.org/10.1002/cjce.5450390106

[8] Tan, J. T., Jing, J. Q., Hu, H. L., You, X. Y. (2018). Experimental study of the factors affecting the flow pattern transition in horizontal oil-water flow. *Experimental Thermal and Fluid Science*, 98, 534-545. https://doi.org/10.1016/j.expthermflusci.2018.06.020

[9] Zhai, L. S., Jin, N. D., Zong, Y. B., Hao, Q. Y., Gao, Z.K. (2015). Experimental flow pattern map, slippage and time–frequency representation of oil–water two-phase flow in horizontal small diameter pipes. *International Journal of Multiphase Flow*, 76, 168-186. https://doi.org/10.1016/j.ijmultiphaseflow.2015.07.007

[10] Zhai, L. S., Zhang, H. X., Cong, Y., Jin, N. D. (2019). Measurement of oil-water interface characteristics in horizontal pipe using a conductance parallel-wire array probe. *IEEE Transactions on Instrumentation and Measurement*, 68 (9), 3232-3243. https://doi.org/10.1109/TIM.2018.2877221

[11] Luo, X. M., Lv, G. B., He, L. M., Lv, Y. L., Zhang, W. (2016). Study on the flow pattern of extra thick oil-water two-phase flow. *Journal of Engineering Thermophysics*, 7 (5), 1005-1010.

[12] He, Y. S., Ren, Y. Y., Han Y. F., Jin, N. D. (2019). Measuring flow pattern asymmetry of oil-water two phase flows using multi-channel rotating electric field conductance signals. *Zeitschrift für Naturforschung A*, 74 (1), 25-41. https://doi.org/10.1515/zna-2018-0312

[13] Qing, M. Y., Liang, H. Q., Zhang, J. J., Zhan, H. L. (2020). The mechanism of detecting water content in oil-water emulsions using impedance spectroscopy. *Journal of Petroleum Science and Engineering*, 188, 106863. https://doi.org/10.1016/j.petrol.2019.106863

[14] Yang, Y. G., Xu, Y., Yuan, C., Wang, J. H., Wu, H. T., Zhang, T. (2021). Water cut measurement of oil–water two-phase flow in the resonant cavity sensor based on analytical field solution method. *Measurement*, 174, 109078. https://doi.org/10.1016/j.measurement.2021.109078

[15] Liu, W., Tan, C., Dong, F. (2021). Doppler spectrum analysis and flow pattern identification of oil-water two-phase flow using dual-modality sensor. *Flow Measurement and Instrumentation*, 77, 101861. https://doi.org/10.1016/j.flowmeasinst.2020.101861

[16] Su, Q., Deng, X. T., Liu, Z. X., Tan, C., Dong. F. (2022). Phase fraction measurement of oil–gas–water three-phase flow with stratified gas by ultrasound technique. *Measurement Science and Technology*, 33, 075302. https://doi.org/10.1088/1361-6501/ac60f6

[17] Bai, L. D., Ma, J., Liu, W. X., Jin, N. D. (2023). Instability of low-velocity and high water-cut oil-water two-phase flow based on microwave signals. *Heat Transfer Engineering*, 44 (16-18), 1578-1590. https://doi.org/10.1080/01457632.2022.2140638

[18] Zhai, L. S., Angeli, P., Jin, N. D., Zhou, D. S., Zhu, L. (2017). The nonlinear analysis of horizontal oil-water two-phase flow in a small diameter pipe. *International Journal of Multiphase Flow*, 92, 39-49. https://doi.org/10.1016/j.ijmultiphaseflow.2017.02.006

[19] Eshrati, M., Al-Wahaibi, T., Al-Hashmi, A. R., Al-Wahaibi, Y., Al-Ajmi, A., Abubakar, A. (2017). Experimental study of drag reduction of polymer-polymer mixtures in horizontal dispersed oil-water flow. *Experimental Thermal and Fluid Science*, 83, 169-176. https://doi.org/10.1016/j.expthermflusci.2017.01.006

[20] Shi, J., Gourma, M., Yeung, H. (2017). CFD simulation of horizontal oil-water flow with matched density and medium viscosity ratio in different flow regimes. *Journal of Petroleum Science and Engineering*, 151, 373-383. https://doi.org/10.1016/J.PETROL.2017.01.022

[21] Gu, M., Jin, N. D., Zhu, L., Gao, Z. K., Zhai, L. S. (2012). Local characteristics of horizontal oil-water two-phase flow: A comparison of CFD simulation and measurement. In *Proceedings of the 31st Chinese Control Conference*. IEEE, 25-27. https://ieeexplore.ieee.org/document/6391154

[22] Gao, H., Gu, H. Y., Guo, L. J. (2003). Numerical study of stratified oil–water two-phase turbulent flow in a horizontal tube. *International Journal of Heat and Mass Transfer*, 46 (4), 749-754. https://doi.org/10.1016/S0017-9310(02)00321-6

[23] Desamala, A. B., Vijayan, V., Dasari, A., Dasmahapatra, A. K., Mandal, T. K. (2016). Prediction of oil-water flow patterns, the radial distribution of volume fraction, pressure and velocity during separated flows in a horizontal pipe. *Journal of Hydrodynamics*, 28, 658-668. https://doi.org/10.1016/S1001-6058(16)60670-4

[24] Dasari, A., Desamala, A. B., Ghosh, U. K., Dasmahapatra, A. K., Mandal, T. K. (2014). Correlations for prediction of pressure gradient of liquid-liquid flow through a circular horizontal pipe. *Journal of Fluids Engineering*, 136 (7), 071302. https://doi.org/10.1115/1.4026582

[25] Li, Y. J., Wang, J., Li, D., Liu, R. G. (2018). Flow pattern diagrams of oil-water two-phase microflows and stable parallel flows obtained at low Reynolds numbers. *International Journal of Multiphase Flow*, 98, 139-146. https://doi.org/10.1016/j.ijmultiphaseflow.2017.09.008

[26] Daneshvar Garmroodi, M. R., Ahmadpour, A. (2020). Numerical simulation of stratified waxy crude oil and water flows across horizontal pipes in the presence of wall heating. *Journal of Petroleum Science and Engineering*, 193, 107458. https://doi.org/10.1016/j.petrol.2020.107458

[27] Mazza, R. A., Suguimoto, F. K. (2020). Experimental investigations of kerosene-water two-phase flow in a vertical pipe. *Journal of Petroleum Science and Engineering*, 184, 106580. https://doi.org/10.1016/j.petrol.2019.106580

[28] Gao, Q. C., Wang, Z. M., Zeng, Q. S. (2021). A unified model of oil/water two-phase flow through the complex pipeline. *Geofluids*, 2021, 3756577. https://doi.org/10.1155/2021/3756577

[29] Bochio, G., Cely, M. M. H., Teixeira, A. F. A., Rodriguez, O. M. H. (2021). Experimental and numerical study of stratified viscous oil–water flow. *Transport Phenomena and Fluid Mechanics*, 67 (6), e17239. https://doi.org/10.1002/aic.17239

[30] Liu, Y. C., Tang, Z.Y., Bai, L. D., Jiang, B., Jin, N. D. (2023). Measurement of inclined oil–water two-phase flows with the combination of electromagnetic flowmeter and differential pressure sensor. *IEEE Sensors Journal*, 23 (18), 21096-21104. https://doi.org/10.1109/JSEN.2023.3302797